Calhoun: The NPS Institutional Archive

DSpace Repository

Theses and Dissertations | 1. Thesis and Dissertation Collection, all items

2012-12

Microstructure and dynamic failure properties of freeze-cast materials for thermobaric warhead cases

Tan, Yi Ming

Monterey, California. Naval Postgraduate School

https://hdl.handle.net/10945/27911

Downloaded from NPS Archive: Calhoun

http://www.nps.edu/library

Calhoun is the Naval Postgraduate School's public access digital repository for research materials and institutional publications created by the NPS community. Calhoun is named for Professor of Mathematics Guy K. Calhoun, NPS's first appointed -- and published -- scholarly author.

Dudley Knox Library / Naval Postgraduate School
411 Dyer Road / 1 University Circle
Monterey, California USA 93943

NAVAL POSTGRADUATE SCHOOL

MONTEREY, CALIFORNIA

THESIS

MICROSTRUCTURE AND DYNAMIC FAILURE PROPERTIES OF FREEZE-CAST MATERIALS FOR THERMOBARIC WARHEAD CASES

by

Yi Ming Tan

December 2012

Thesis Advisor: Joseph Hooper

Approved for public release; distribution is unlimited

THIS PAGE INTENTIONALLY LEFT BLANK

REPORT DOCUMENTATION PAGE			Form Approved OMB No. 0704–0188
Public reporting burden for this collection of information is estimated to average 1 hour per response, including the time for reviewing instruction, searching existing data sources, gathering and maintaining the data needed, and completing and reviewing the collection of information. Send comments regarding this burden estimate or any other aspect of this collection of information, including suggestions for reducing this burden, to Washington headquarters Services, Directorate for Information Operations and Reports, 1215 Jefferson Davis Highway, Suite 1204, Arlington, VA 22202–4302, and to the Office of Management and Budget, Paperwork Reduction Project (0704–0188) Washington DC 20503.			
1. AGENCY USE ONLY ***(Leave blank)***	**2. REPORT DATE** December 2012	**3. REPORT TYPE AND DATES COVERED** Master's Thesis	
4. TITLE AND SUBTITLE MICROSTRUCTURE AND DYNAMIC FAILURE PROPERTIES OF FREEZE-CAST MATERIALS FOR THERMOBARIC WARHEAD CASES		**5. FUNDING NUMBERS**	
6. AUTHOR(S) Yi Ming Tan			
7. PERFORMING ORGANIZATION NAME(S) AND ADDRESS(ES) Naval Postgraduate School Monterey, CA 93943–5000		**8. PERFORMING ORGANIZATION REPORT NUMBER**	
9. SPONSORING /MONITORING AGENCY NAME(S) AND ADDRESS(ES) N/A		**10. SPONSORING/MONITORING AGENCY REPORT NUMBER**	
11. SUPPLEMENTARY NOTES The views expressed in this thesis are those of the author and do not reflect the official policy or position of the Department of Defense or the U.S. Government. IRB Protocol number ____N/A____.			
12a. DISTRIBUTION / AVAILABILITY STATEMENT Approved for public release; distribution is unlimited		**12b. DISTRIBUTION CODE** A	

13. ABSTRACT (maximum 200 words)

We consider the microstructure and dynamic failure of ice-templated freeze cast alumina materials that are currently being studied for novel warhead cases. The freeze-cast matrix is a porous, cellular structure of overlapping lamellae similar to many biomaterials such as nacre. This lightweight matrix provides a high-toughness shell that can be filled with polymers or combustible reactive materials. Three porosities of alumina freeze-cast structures were studied, and a systematic variation in microstructural properties such as lamellar width and thickness was observed with changing porosity. Dynamic impact tests were performed in a single stage light-gas gun to examine the failure properties of these materials under high strain-rate loading. Nearly complete delamination was observed under impact, along with characteristic cracking across the lamellar width. Average fragment size decreases with increasing porosity, and a theoretical model was developed to explain this behavior. Based on an energy balance between kinetic, strain, and surface energies within a single lamella, we are able to predict the characteristic fragment size using only standard material properties of bulk alumina.

14. SUBJECT TERMS reactive materials, fragmentation, explosives, warheads, advanced materials, freeze-cast			**15. NUMBER OF PAGES** 61
			16. PRICE CODE
17. SECURITY CLASSIFICATION OF REPORT Unclassified	**18. SECURITY CLASSIFICATION OF THIS PAGE** Unclassified	**19. SECURITY CLASSIFICATION OF ABSTRACT** Unclassified	**20. LIMITATION OF ABSTRACT** UU

NSN 7540–01–280–5500

Standard Form 298 (Rev. 2–89)
Prescribed by ANSI Std. 239–18

THIS PAGE INTENTIONALLY LEFT BLANK

Approved for public release; distribution is unlimited

MICROSTRUCTURE AND DYNAMIC FAILURE PROPERTIES OF FREEZE-CAST MATERIALS FOR THERMOBARIC WARHEAD CASES

Tan, Yi Ming
Civilian, Defence Science and Technology Agency (Singapore)
B.Eng (Mechanical Engineering), National University of Singapore, 2005

Submitted in partial fulfillment of the
requirements for the degree of

MASTER OF SCIENCE IN APPLIED PHYSICS

from the

NAVAL POSTGRADUATE SCHOOL
December 2012

Author: Tan, Yi Ming

Approved by: Dr. Joseph Hooper
Thesis Advisor

Dr. Andres Larraza
Chair, Department of Physics

THIS PAGE INTENTIONALLY LEFT BLANK

ABSTRACT

We consider the microstructure and dynamic failure of ice-templated freeze cast alumina materials that are currently being studied for novel warhead cases. The freeze-cast matrix is a porous, cellular structure of overlapping lamellae similar to many biomaterials such as nacre. This lightweight matrix provides a high-toughness shell that can be filled with polymers or combustible reactive materials. Three porosities of alumina freeze-cast structures were studied, and a systematic variation in microstructural properties such as lamellar width and thickness was observed with changing porosity. Dynamic impact tests were performed in a single stage light-gas gun to examine the failure properties of these materials under high strain-rate loading. Nearly complete delamination was observed under impact, along with characteristic cracking across the lamellar width. Average fragment size decreases with increasing porosity, and a theoretical model was developed to explain this behavior. Based on an energy balance between kinetic, strain, and surface energies within a single lamella, we are able to predict the characteristic fragment size using only standard material properties of bulk alumina.

THIS PAGE INTENTIONALLY LEFT BLANK

TABLE OF CONTENTS

I. INTRODUCTION 1
- **A. MOTIVATION 1**
- **B. OBJECTIVES 2**

II. BACKGROUND 3
- **A. REACTIVE MATERIALS 3**
- **B. FRAGMENTATION 3**
- **C. FREEZE CAST MATERIALS 5**
  - **1. Freeze Casting Process 5**
    - ***a. Step 1: Preparation of the Slurry 6***
    - ***b. Step 2: Controlled Solidification of the Slurry 6***
    - ***c. Step 3: Sublimation of the Solvent 7***
    - ***d. Step 4: Sintering of the Green Body 7***
  - **2. Ice-Templated Freeze Cast Materials 7**
  - **3. Surface Roughness of Lamellae 8**
  - **4. Properties 9**

III. MORPHOLOGY OF FREEZE CAST MATERIALS 11
- **A. SAMPLE 11**
- **B. ALUMINA POWDER MORPHOLOGY 11**
- **C. GENERAL FEATURES OF THE MICROSTRUCTURE 13**

IV. EXPERIMENTAL METHODOLOGY 19
- **A. SAMPLE PREPARATION 19**
- **B. LOW VELOCITY GAS GUN IMPACT TEST 20**
- **C. SIEVING PROCESS 21**

V. TEST RESULTS AND ANALYSIS 23
- **A. INITIAL TEST CONDITIONS 23**
- **B. FRAGMENT DISTRIBUTIONS 23**
- **C. MICROSTRUCTURE ANALYSIS OF FRAGMENTS 24**
- **D. FRAGMENTATION MODEL 30**

VI. CONCLUSIONS AND RECOMMENDATIONS 35
- **A. CONCLUSIONS 35**
- **B. RECOMMENDATIONS 35**

APPENDIX 37
- **C. RAW DATA FOR 46–54-S1 EXPERIMENT 37**
- **D. RAW DATA FOR 60–40-S1 EXPERIMENT 38**
- **E. RAW DATA FOR 75–25-S1 EXPERIMENT 39**

LIST OF REFERENCES 41

INITIAL DISTRIBUTION LIST 43

THIS PAGE INTENTIONALLY LEFT BLANK

LIST OF FIGURES

Figure 1. Freeze cast process: slurry preparation, solidification, sublimation and sintering (From Ref 6). 6
Figure 2. (a) Crystal structure of ice, (b) anisotropy of crystal growth kinetics, leading to lamellar ice crystals. The anisotropy of the growth kinetics is reflected in the final porous structures (c) obtained after sublimation and sintering. The direction perpendicular to the ceramic platelets corresponds to the limited growth direction of ice crystals (From Ref 6).....8
Figure 3. Dendritic surface of (a) alumina using water as a solvent (b) silicon nitride using water as a solvent (From Ref 6).....9
Figure 4. Photo of freeze cast sample (OC-FC-039A).....11
Figure 5. SEM micrographs of alumina powder (a) sintered and (b) unsintered.....12
Figure 6. Powder particle size distribution results from the HORIBA. 13
Figure 7. SEM micrograph showing the microstructure of samples with different porosity. The cross-section is parallel to the ice front. Total porosity of (a) 46 % (b) 60% (c) 75%. 14
Figure 8. SEM micrograph of (a) ceramic lamellae with dense microstructure (b) high magnification of lamella showing the densely packed alumina grains. ..15
Figure 9. SEM micrograph of a ceramic bridge observed in a 46% porosity sample.....15
Figure 10. Physical parameters of freeze cast samples of varying porosity.....16
Figure 11. Lamellar width of freeze cast samples.....17
Figure 12. Freeze cast sample (60-40-S1) bonded to the anvil. 19
Figure 13. Fragmentation containment unit, assembled photo (From Ref. 5). 20
Figure 14. Schematic illustrating the fragmentation containment unit. 21
Figure 15. Typical sieve stack (From Ref. 5).....22
Figure 16. Mass PDF vs. size for freeze cast material with different porosity. 24
Figure 17. SEM micrograph of 4.75mm fragment for porosity of 46%. 25
Figure 18. SEM micrograph of 500μm fragment for porosity α = (a) 46% (b) 60% (c) 75%. 27
Figure 19. SEM micrograph of 500μm fragment for sample of porosity α = 46% showing crack bridging and blunting at a dendritic ridge.....28
Figure 20. SEM micrograph of (a) 500μm fragment for sample of porosity α = 46% (b) 55μm fragment for sample of porosity α = 75%. Multi-mode cracking mechanism is observed. 29
Figure 21. Schematic of the energy balance model for a cylindrical fragment formed within a detached lamella.....30
Figure 22. Average fragment size vs. lamellar width ω.....34

THIS PAGE INTENTIONALLY LEFT BLANK

LIST OF TABLES

Table 1. Summary of BET measurements. 17
Table 2. Sample dimensions. 23
Table 3. Shot table. 23
Table 4. Material properties used in the fragmentation model. 33

THIS PAGE INTENTIONALLY LEFT BLANK

LIST OF ACRONYMS AND ABBREVIATIONS

CDF	Cumulative Distribution Function
LLNL	Lawrence Livermore National Laboratory
PDF	Probability Density Function
PMMA	Poly(Methyl Methacrylate)
RM	Reactive Materials
SEM	Scanning Electron Microscope

THIS PAGE INTENTIONALLY LEFT BLANK

ACKNOWLEDGMENTS

First I would like to thank my fiancé and my family, without their continued support I would not have been able to accomplish this achievement.

Next, I would like to express my deepest gratitude to my thesis advisor, Professor Joseph Hooper for his guidance, patience and support. His leadership and sincerity inspired me throughout my research and study. Throughout his busy schedule, he always takes time off to answer my questions and clarify the scope of my research.

To my thesis group, I would also like to thank them for all the help rendered during the preparation of all the experiments and the time spent in the lab would not have been as fun if not for them.

I would also like to thank Professor Sareth Menon, Professor Luke Brewer, Professor Claudia Luhrs, Dr. Chanman Park and Dr. Dong Jin Woo for all their help in the guidance provided in the analysis conducted for my research.

Finally, I would like to thank Dr. Octavio Cervantes and John Molitoris from Energetic Materials Center at Lawrence Livermore National Laboratory for providing for all their help in the synthesis of the freeze cast samples and answering all my queries.

THIS PAGE INTENTIONALLY LEFT BLANK

I. INTRODUCTION

A. MOTIVATION

In this thesis we consider the morphology and dynamic failure of ice-templated freeze cast materials for novel warhead casings. The freeze casting process used in this work involves freezing, sublimating and sintering an alumina/water slurry to create a cellular, porous alumina structure. This porous template can then be filled with other materials, such as elastomeric polymers for additional lightweight support. In collaboration with researchers at Lawrence Livermore National Laboratory, we are considering the use of these templates as novel ways to create reactive material (RM) composites. RMs are energetic compounds that are insensitive under normal conditions but can undergo rapid combustion under dynamic loading from a shock wave or high-velocity impact. RM composites increase the lethality of a warhead either by providing additional fuel for post-detonation combustion and enhanced blast, or by generating reactive fragments that burn after striking a secondary target. Many are designed to replace traditional steel or aluminum components in warheads or missile casings, adding additional lethality from metal combustion without significant increases to weight. Successful infiltration of a reactive metal into a freeze-cast shell may provide a tough, lightweight material than will generate small fragments with significant metal surface area under explosive loading. Previous work on freeze cast materials, both filled and unfilled, has been limited mainly to static loading; here our goal is to understand the relationship between the microstructure of freeze-cast reactive materials and their fracture and fragmentation properties under rapid loading such as would occur in warhead environments.

Fragmentation and post-mortem recovery is essential in determining the failure properties and, ultimately, the lethality from RM casings. In the freeze casting process, the porosity of the material is a direct replica of the solvent content and can be systematically varied over a wide range of values. The change in porosity may also be linked to changes in microstructural morphology, such as the dimensions of the cellular structure. The manner in which porosity and microstructural changes affect dynamic

fracture has, to our knowledge, not been examined in these materials. An improved understanding of these fundamental properties of freeze-cast matrices will allow for better synthesis efforts when reactive materials are incorporated into the porous regions.

B. OBJECTIVES

The objectives of this thesis are to analyze the microstructure of freeze cast materials of different porosities, examine their fragmentation properties under dynamic loading, and establish a relationship between the microstructure and the fragmentation properties.

II. BACKGROUND

A. REACTIVE MATERIALS

Reactive materials are generally solid energetic materials that are insensitive to shock and heat as compared to common organic explosives and propellants. When subjected to dynamic loading or extremely high temperatures, reactive materials release significant amounts of energy through standard combustion processes. This release of energy occurs over much slower timescales than typical detonation or deflagration waves. While a wide range of materials could feasibly fall into this category, recent Navy interest has focused on combustible metals with high energy densities. Fragment clouds of metallic RM warhead casings can improve the overall blast impulse and lethality at secondary targets as compared to standard case materials. While a number of large-scale tests have demonstrated improved lethality against realistic targets when using reactive material casings, there is limited understanding of many of their basic physical properties, particularly in the areas of combustion and fragmentation.

B. FRAGMENTATION

One of the key pieces of experimental data in this thesis is recovered fragment distributions from freeze-cast matrices following dynamic loading. In this section we present some of the basic analytic analysis used in understanding high strain-rate fragmentation. In the case of reactive materials, the size distribution of fragments (and thus their surface area) has a dramatic effect on the combustion and lethality properties of the case. Our goal is both to understand the experimentally collected data and also inform a theoretical model to predict an average fragment size from fragmentation of a freeze-cast matrix.

The simplest geometric fragment distribution is the exponential or Lineau[1] distribution, where the location of random breaks or fracture points in a warhead case is described by Poisson statistics. Consider a length of warhead case, unrolled into a one-dimensional line. Fractures along this line create one side of a fragment, and their appearance is assumed to be fully uncorrelated. The probability of locating *n* number of

fractures within the length l in a the warhead case with an average spacing between breaks λ is

$$P(n,l) = \frac{(l/\lambda)^n e^{-l/\lambda}}{n!}.$$

The probability of having no fractures within a length l is

$$P(0,l) = e^{-l/\lambda}.$$

The probability of finding a single fracture in the differential length dl is

$$P(l,dl) = \frac{1}{\lambda} dl.$$

Combining these two expressions gives the fragment length probability density function (PDF) describing the number distributions of fragments over their length

$$f(l) = \frac{1}{\lambda} e^{-l/\lambda}.$$

The corresponding cumulative distribution function (CDF) for the number of fragments of a length less than or equal to l is

$$F(l) = 1 - e^{-l/\lambda}.$$

The only parameter in this distribution is the average fragment size. This can either be a fit parameter or estimated from a number of theoretical models. One common approach was introduced by Grady, who used an energy-based relation relating fragment number to fracture toughness. In the Grady[1] model the kinetic energy and strain energy of an expanding sphere of mass is balanced against the energy required to form a new fracture surface. A surface spontaneously forms and the relation to the average fragment length is

$$x_o = \left(\frac{\sqrt{12} K_f}{\rho c \dot{\varepsilon}} \right)^{\frac{2}{3}},$$

where ρ is the density of the fragmented material, c is the longitudinal sound speed, $\dot{\varepsilon}$ is the strain rate, and K_f is the dynamic fracture toughness.

In what follows, we use the Lineau distribution to treat the quasi-1D fragmentation of lamella within the freeze-cast matrix. In the spirit of Grady's model, we develop a new energy balance theory to treat the fragmentation of our freeze cast composites, and compare the predicted size to fits of experimental data with the Lineau distribution. Additional details are given in the experimental results section.

C. FREEZE CAST MATERIALS

Freeze casting technology combines compounds such as aluminum oxide and poly(methyl methacrylate) (PMMA) to develop a cellular porous structure. In this process, the ceramic powder is mixed with a solvent, forming a suspension. The suspension is frozen and then sublimated to remove the solvent, leaving behind a porous template. The porosity is a direct replica of the solvent when in solid state in the suspension. Subsequently, the porous structure can be infiltrated with a variety of materials, such as a standard polymer like PMMA. This hybrid material is believed to exhibit high specific strength and toughness and at the same time, is lightweight and able to withstand high temperatures.[6, 7] Nacre, a natural material that is a strong and tough coating on shells, is an inspiration to the research into the freeze-casted materials. When water is used as the solvent for the freeze casting process, a layered structure with dendritic features on the surface of the layers is formed. The dendrites provide roughness to the surface. Filling the structure with polymer increases the material's toughness through several energy dissipation mechanisms, including uncracked-ligament bridging and frictional sliding along the rough dendritic surface[7,8]. The freeze casting process produces well-controlled pore structures, hence providing an advantage over other conventional methods of making porous ceramics[9].

1. Freeze Casting Process

In freeze casting, the process can be divided into four steps, illustrated in Figure 1.

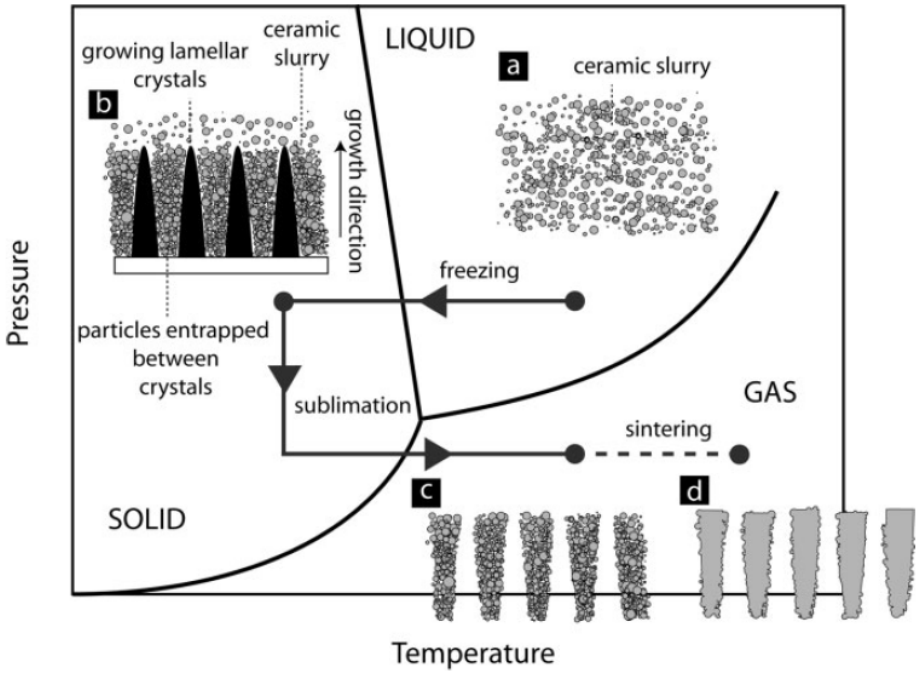

Figure 1. Freeze cast process: slurry preparation, solidification, sublimation and sintering (From Ref 6).

a. Step 1: Preparation of the Slurry

The ceramic powder is dispersed in the solvent. A binder is added to provide strength to the structure. This is essential because after the solvent is removed during the sublimation stage, the green bodies can collapse if there is no binder.

b. Step 2: Controlled Solidification of the Slurry

During this critical step, continuous crystals of solvent are formed, under certain conditions, and grow into the slurry. Ceramic particles in suspension in the slurry are expelled by the moving solidification front, concentrated and entrapped in-between the crystals. To achieve this natural segregation, the slurry is poured in a mold, which undergoes isotropic or anisotropic cooling to induce homogeneous or directional solidification. The solidification conditions are selected based on the initial choice of the solvent. The device should also accommodate the solidification volume change. The temperature of the mold is regulated to control the speed of the solidification front. The

cooling conditions will determine the characteristics of the growing solvent crystals and hence the final characteristics of the porosity.

c. Step 3: Sublimation of the Solvent

When the sample is completely solidified, it is kept at low temperature and reduced pressure, sublimation conditions determined by the physical properties of the solvent. The solidified solvent is then converted into gas, leaving behind a porous green body.

d. Step 4: Sintering of the Green Body

Once the solvent has been totally removed, the obtained green body can be sintered with a conventional sintering technique. The low strength of the green body prevents any use of pressure assisted sintering. Due to the low amount of binder used, no additional binder burnout process is required. During the sintering stage, the macroporosity created by the solvent crystals is retained while the microporosity is eliminated from the ceramic walls.

2. Ice-Templated Freeze Cast Materials

In this section, we discuss freeze materials where water is used as the solvent. Water is one of the most easily available solvents for the process, and all samples produced for this work at LLNL used this manner of ice-templating to form the final freeze-cast matrix. The microstructure in this case has a lamellar structure in which the ceramic layers are parallel to each other and very homogeneous throughout the entire sample. Particles trapped in between the ice dendrites lead to a dendritic surface roughness of the walls, just as in nacre.

The morphology of ice-templated freeze cast material[6] can be described based on the basic crystallographic (Figure 2(a)) and crystal growth characteristics of ice. The ice front velocity perpendicular to the crystallographic *c* axis is much higher than the ice front velocity parallel to this axis (Figure 2(b)). Thus the ice crystals will grow much faster along the *a* axis, creating a highly anisotropic structure. The thickness of the ice crystals that is along the *c* axis will remain small.

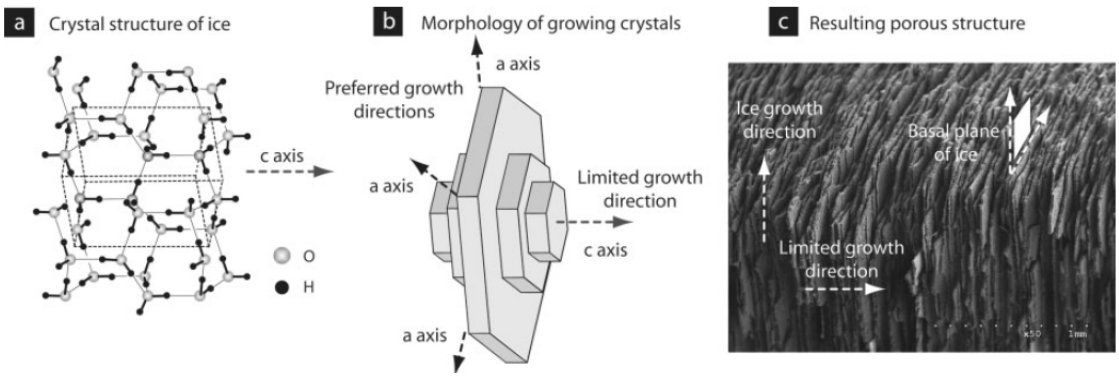

Figure 2. (a) Crystal structure of ice, (b) anisotropy of crystal growth kinetics, leading to lamellar ice crystals. The anisotropy of the growth kinetics is reflected in the final porous structures (c) obtained after sublimation and sintering. The direction perpendicular to the ceramic platelets corresponds to the limited growth direction of ice crystals (From Ref 6).

3. Surface Roughness of Lamellae

The surface of the lamellae in ice-templated materials shows dendritic-like features (Figure 3), a result of the ice formation. These dendritic-like features have generally uniform size and distribution through the lamellae and run along the solidification direction. It is observed that the surface roughness is found only on one side of the lamellae. This is mainly due to the growth pattern of ice crystals[10]. In general, since the roughness is directly related to the morphology of the solvent crystal, every solvent will yield a different roughness.

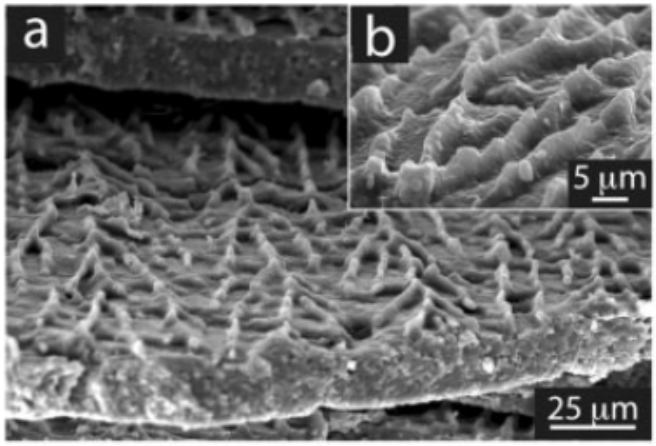

Figure 3. Dendritic surface of (a) alumina using water as a solvent (b) silicon nitride using water as a solvent (From Ref 6).

4. Properties

Several studies have indicated that freeze-cast ceramics have higher compressive strength than their individual material components. This is attributed to the morphology of the pores obtained. In an alumina and PMMA ice-templated material, it is found that the plane strain K_{Ic} fracture toughness is almost double compared to a non-freeze cast alumina-PMMA mixture[7].

In the alumina-PMMA matrix or similar form of ceramic-polymer matrix, there are two main forms of deformation: inelastic deformation within the polymer layers and microcracks within the ceramic layers. These ductile and brittle deformations appear to be distinct, with little evidence of interaction. Uncracked-ligament bridges can be formed if these distinct ductile and brittle deformations are triggered ahead of the main growing crack. To break these bridges, energy is required and this reduced the crack tip advancement and leads to ductile-phase toughening. The elongated voids in the polymer layers function as a crack arrester too. In the lamellar structures, the crack deflection and "delamination" along the interface promotes the formation of uncracked-ligament bridging, as well as frictional sliding along the rough delaminated interface. This increases the toughness of the material through energy dissipation within the soft phase[7]. Hence such materials with an ice-templated structure display a higher toughness when compared to simple mixture of their constituents.

With their high compressive strength and toughness, we are (in collaboration with LLNL) interested in exploring the feasibility of using freeze-cast materials in warhead casings. The porosity of these templates allows them to be infiltrated by metals for extra strength and combustion energy release, but initially our goal is to investigate the plain freeze-casted material with no infiltration to gain a better appreciation of the fragmentation behavior of this ceramic material with a unique structure.

III. MORPHOLOGY OF FREEZE CAST MATERIALS

A. SAMPLE

In this thesis, we will be examining the microstructure and dynamic failure properties of three freeze cast materials provided by the Energetic Materials Center at Lawrence Livermore National Laboratory (LLNL). All are made of alumina, but with differing pore content and microstructure. All freeze cast samples considered here were synthesized in using water as the solvent, so that the porosity of each type of sample is directly related to the volume of water in the suspension of the starting slurry. Three different porosities (46%, 60%, and 75%) are considered in this study. Figure 4 shows a sample of one of the raw freeze cast cylinders.

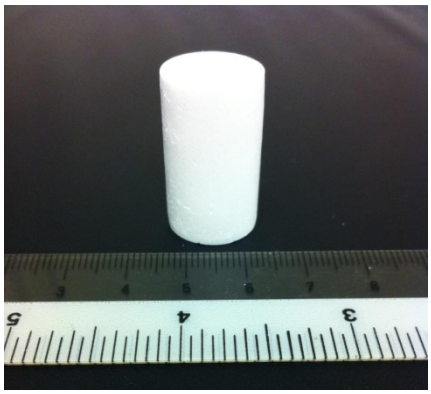

Figure 4. Photo of freeze cast sample (OC-FC-039A).

B. ALUMINA POWDER MORPHOLOGY

The microscopic structure of each freeze cast sample and a reference alumina powder sample were characterized by a Zeiss Neon 40 field emission FIB-SEM. Electron microscopy images were processed using ImageJ 1.46r software to evaluate microstructural properties. We first consider our alumina powder samples, which contain identical particles as those used for the ice-templated matrices. The SEM images of the two types of powder, one sintered and one unsintered, are shown in Figure 5. The powder was compared to those used by S. Deville etc[5] and the images show the similarity in the morphology of the powder. Thermal etching due to the sintering process is observed on

the majority of the alumina grains. In general the morphology of our starting powder is essentially identical to that of previous work. The powder particle size was also measured using a Horiba Laser Scattering Particle Size Distribution Analyzer LA-950. Figure 6 shows the measured particle size distribution. There are two peaks observed in the particle size distribution; the first peak at 141.5 nm corresponds to the intrinsic particle size while the second peak at 1.510 μm is due to agglomeration of the powder.

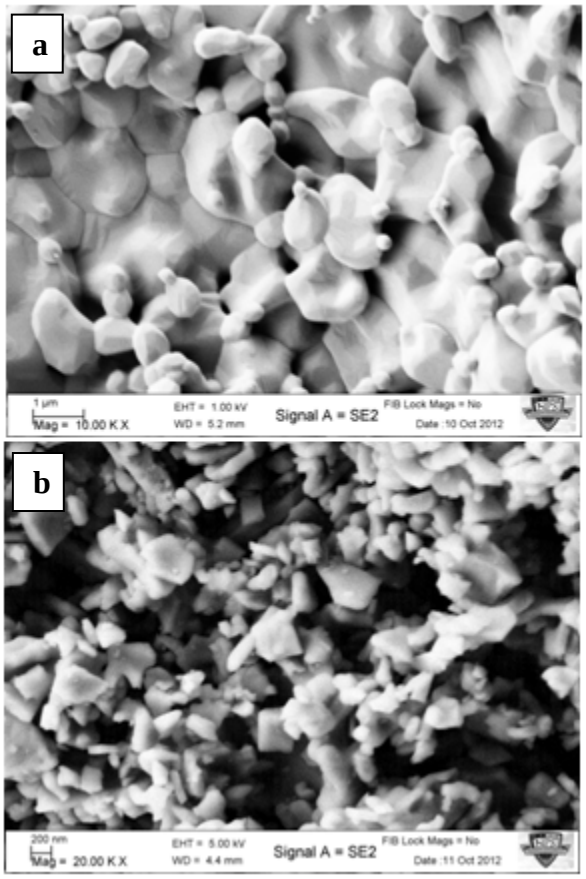

Figure 5. SEM micrographs of alumina powder (a) sintered and (b) unsintered.

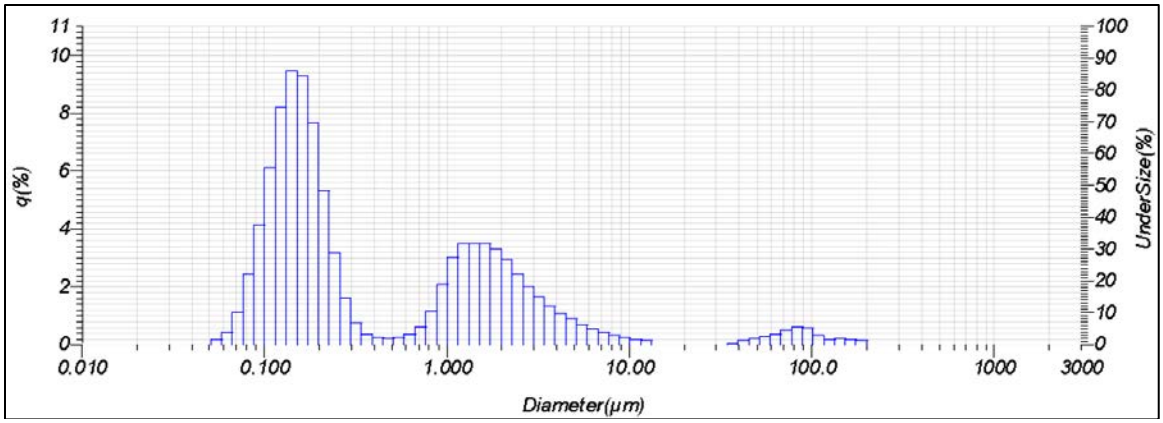

Figure 6. Powder particle size distribution results from the HORIBA.

C. GENERAL FEATURES OF THE MICROSTRUCTURE

The morphology of the cellular freeze-cast materials is closely related to the crystallographic and crystal growth characteristics of ice. Figure 7 shows representative SEM micrographs of the three porosities under consideration in this work. Lamellae and channels are observed in the freeze cast samples. The orientation of the lamellae is generally parallel to the direction of the solidification. The alumina particles within each lamella are densely packed and exhibit terracing due to thermal etching from the sintering process (Figure 8). Minimal residual porosity is observed within the lamellae themselves. The surface of the lamellae contains dendritic features, which range from 3 to 12 μm high depending on the porosity level of the sample. It is also observed, consistent with previous literature, [10] that the dendritic surface features are found only on one side of the lamellae while the other surface remains smooth.

One additional microstructural feature that is more prominent in the lowest porosity sample is the trans-lamellar ceramic bridges (Figure 9). A large number of small bridging structures can be observed between adjacent lamellae; this is distinct from the dendritic structure mentioned in the previous paragraph. The formation of these ceramic bridges is due to trapping of ceramic particles by the growing ice[7].

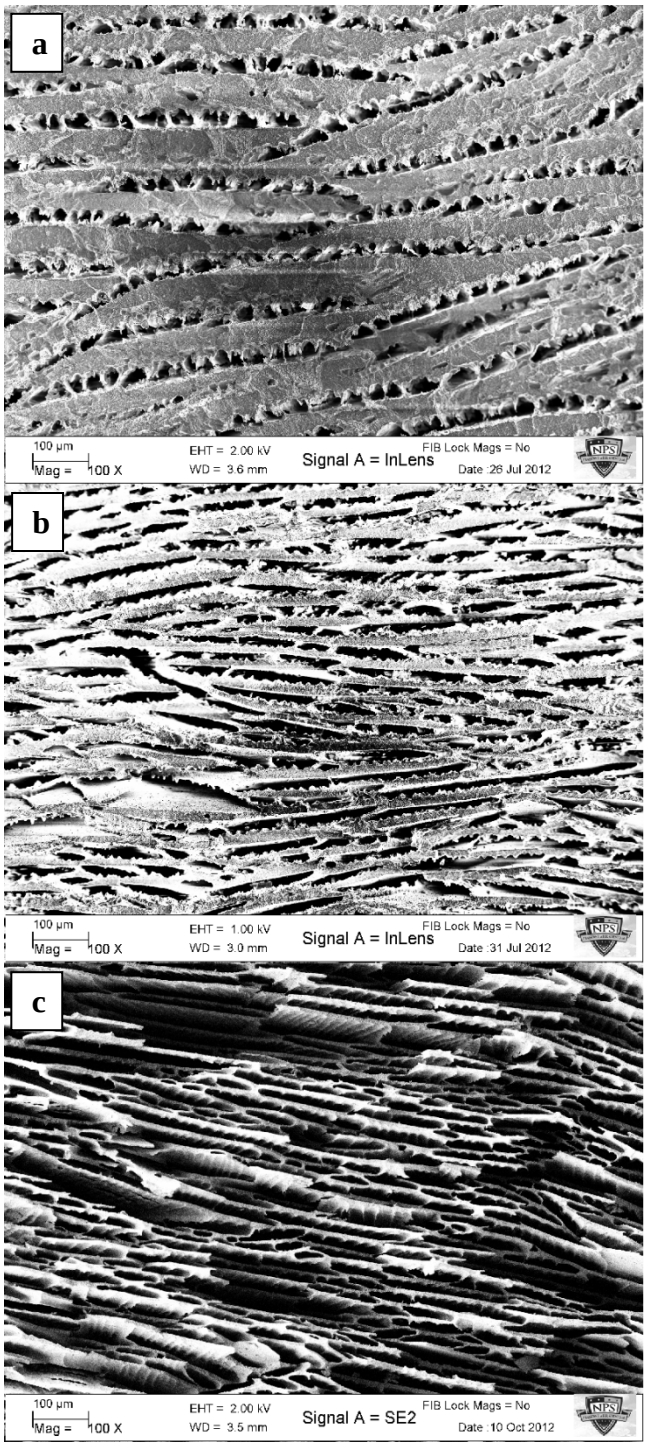

Figure 7. SEM micrograph showing the microstructure of samples with different porosity. The cross-section is parallel to the ice front. Total porosity of (a) 46 % (b) 60% (c) 75%.

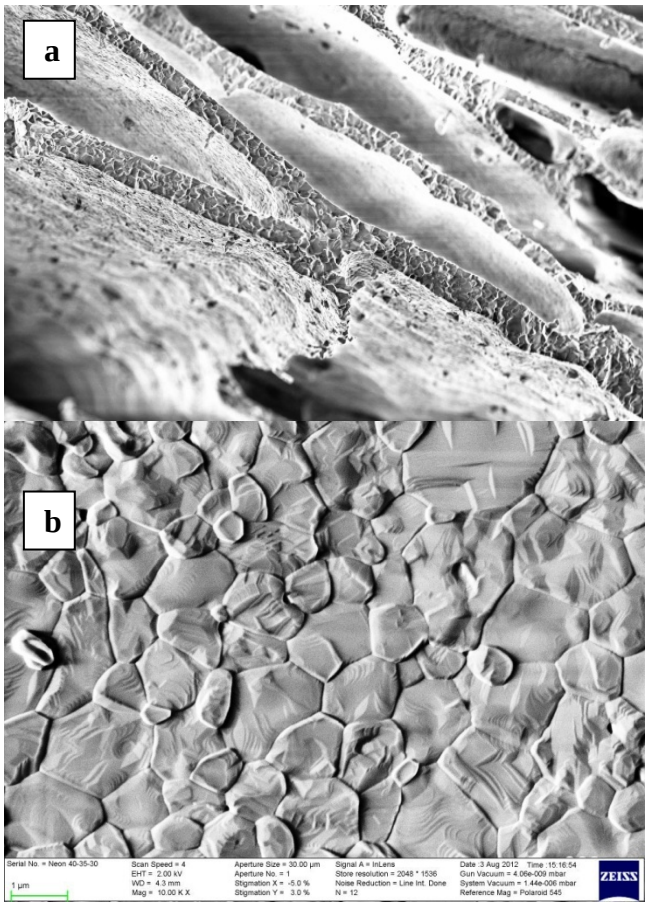

Figure 8. SEM micrograph of (a) ceramic lamellae with dense microstructure (b) high magnification of lamella showing the densely packed alumina grains.

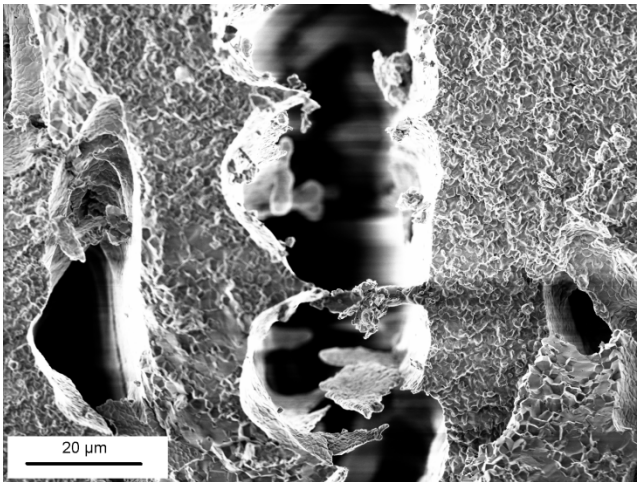

Figure 9. SEM micrograph of a ceramic bridge observed in a 46% porosity sample.

We next consider the variation in microstructure as the porosity changes. Six main characteristics were taken from measurements over multiple SEM images: the alumina grain diameter, the size of porous channels between lamellae, the lamellar thickness, the width of lamellae perpendicular to the solidification front direction, the height of the dendritic surface ridges and finally the spacing between ridges on the surface of the lamella. Figure 10 and 11 summarize the dimensions measured from a large number of SEM micrographs of the three samples. The grain diameter for the three samples is observed to be relatively consistent with an average diameter of 1.7 μm. This is also similar to the grain diameter of the sintered alumina powder.

In all other parameters measured (other than the distance between the ridges), there is a trend observed where the dimensional values decrease with increasing porosity. The width of the lamella, for example, is defined as a distance between junctions or interfaces between lamellae and decreases rapidly with increasing porosity (Figure 11). When handling the three types of samples, it was also noted that the sample with the highest porosity is considerably more brittle compared to the lowest porosity sample. This is likely related to the thickness of the lamellae in the samples. No lamellar length is measured, but we have extracted SEM images of fragments and observed that the relative length of the lamellae is much greater than their width.

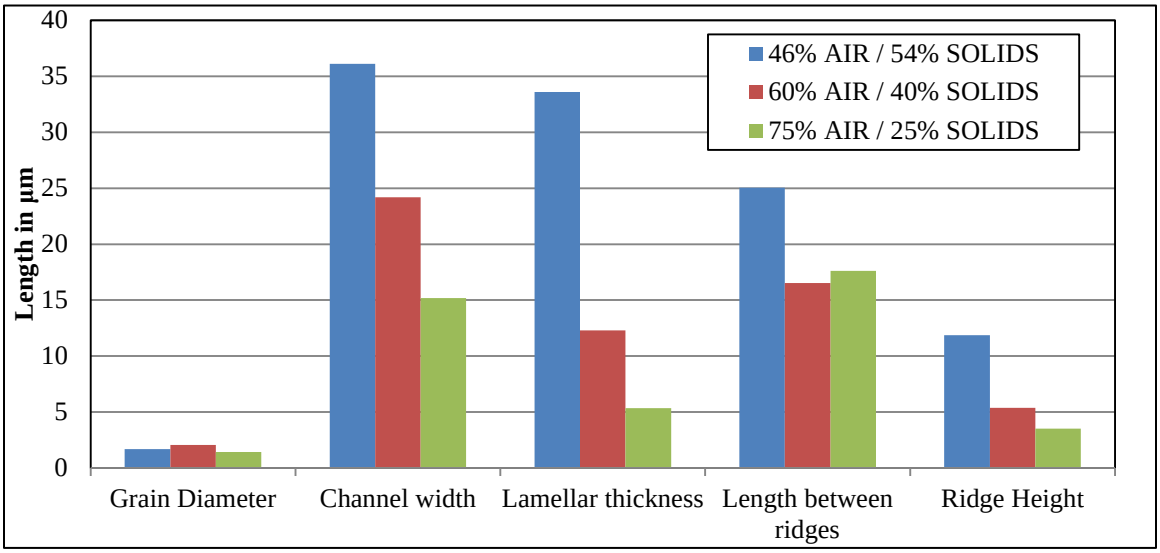

Figure 10. Physical parameters of freeze cast samples of varying porosity.

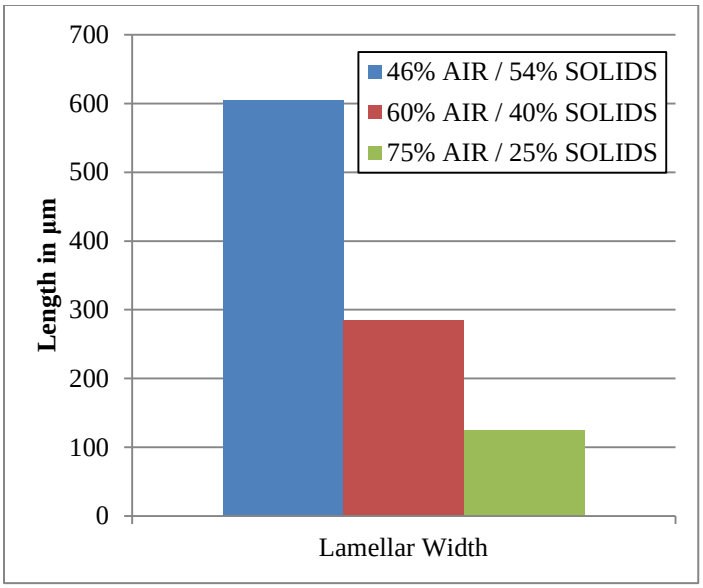

Figure 11. Lamellar width of freeze cast samples.

Surface area and porosity are key physical parameters that will greatly affect future efforts to infiltrate this material with reactive metals. To obtain a specific surface area, BET measurements were performed using a Quantachrome Instruments Nova 4200e Surface Area and Pore Size Analyzer, measuring the nitrogen adsorption isotherm at 77 K. Before measurement, the samples were degassed at 300 °C for 2.5 hours. The surface areas were obtained from the adsorption isotherms. Two runs were conducted for all three samples to ensure consistency in the results. Table 1 summarizes the results for the samples. The average surface area results indicated that with increasing porosity the surface area also increases, as would be expected.

Table 1. Summary of BET measurements.

Sample	**Porosity (%)**	**Average Surface Area (m^2/g)**
OC-FC-039A	46	0.638
OC-FC-042A	60	0.889
OC-FC-040D	75	1.423

THIS PAGE INTENTIONALLY LEFT BLANK

IV. EXPERIMENTAL METHODOLOGY

To investigate the fragmentation properties of the freeze cast material, low velocity gas gun impact tests were conducted on the freeze cast samples. The impact test uses a gun-propelled projectile to impact an intermediate striker bar which rapidly crushes the sample then unloads the stress. Fragments are fully contained with a chamber to allow for post-mortem recovery and analysis.

A. SAMPLE PREPARATION

Ice-templated alumina freeze-cast structures were prepared at LLNL, and were cut to smaller dimensions using a high speed diamond saw. Due to the brittleness of the samples, achieving samples of precisely identical height was challenging. However, the difference in height did not affect the subsequent experimentation, and all fragment distributions were normalized to the total mass collected from the sample. Each sample for fragmentation testing was bonded onto the anvil in the containment unit by epoxy as seen in Figure 12. With the limited samples available, the sample was orientated with the lamellar layers parallel to the axis of impact to investigate the dynamic failure properties of the freeze cast sample in its most susceptible orientation.

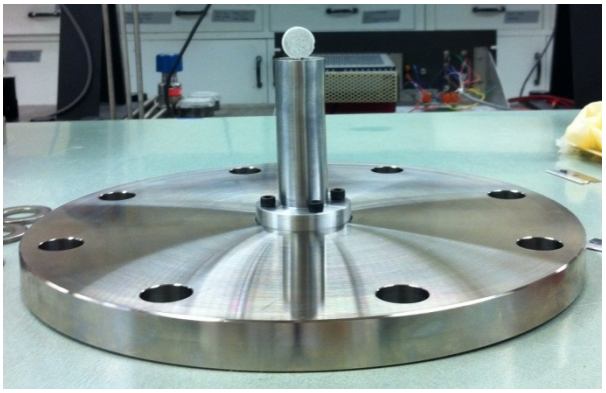

Figure 12. Freeze cast sample (60-40-S1) bonded to the anvil.

B. LOW VELOCITY GAS GUN IMPACT TEST

The test setup and standard operating procedure for the low velocity gas gun impact test is also based on the apparatus and test procedure developed previously by Roderick Wilson[5]. The sample is held within a fragmentation containment unit (Figure 13) so that all fragment particles from the impact test could be collected.

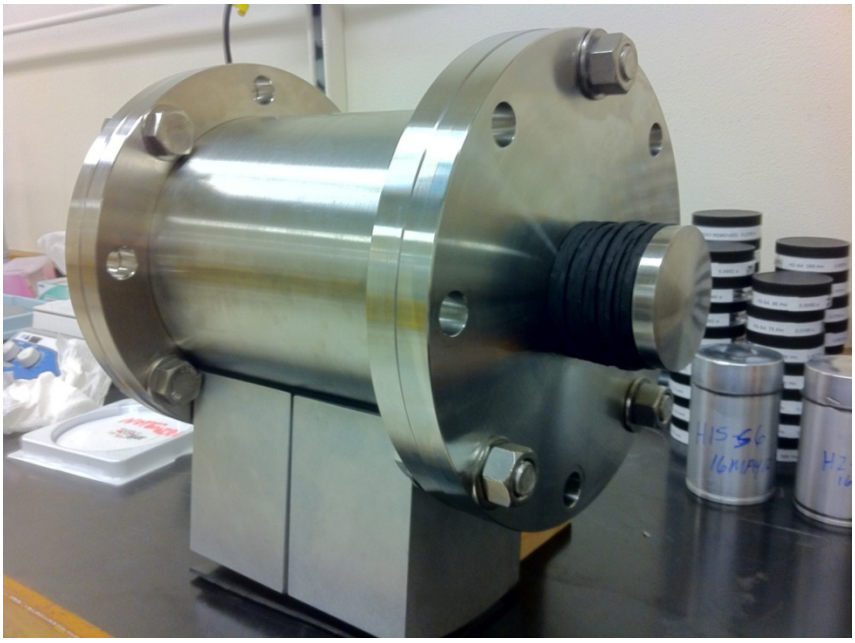

Figure 13. Fragmentation containment unit, assembled photo (From Ref. 5).

A schematic of the fragmentation containment unit is shown in Figure 14. Flat aluminum impactors were launched from a 3” light-gas gun and impacted the striker bar. The bar was guided by brass bushings in the front flange and rapidly impacted and fragmented the sample; a layer of rubber was used to allow the striker bar to unload stress and prevent full compression of the sample. All freeze-cast samples fragmented severely under this rapid loading, and the small particles resulting from this event were carefully removed from the chamber.

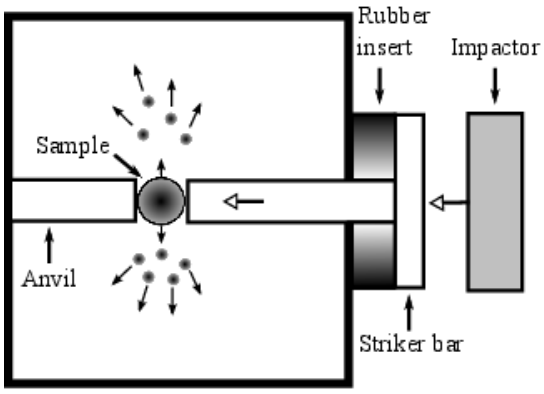

Figure 14. Schematic illustrating the fragmentation containment unit.

C. SIEVING PROCESS

Fragments were collected post-shot and carefully sieved to determine their mass distribution as a function of a linear particle size. A standard sieve stack (Figure 15) was used; this consists of a nested column of sieves with wire mesh screens, in which each screen will allow only particles of that specific size or smaller to pass through. The top sieve has the largest holes in the mesh screen while each lower sieve has a smaller screen opening. The contents of each sieve are weighed in a microbalance, giving the necessary data required for a mass probability density function distributed over linear size.

Figure 15. Typical sieve stack (From Ref. 5).

To prevent secondary fragmentation from occurring, each sieve was gently shaken by hand when sifting the samples. The sieves used for these experiments ranged from 4.75 mm down to 45 microns (4.75 mm, 2.8 mm, 1.7 mm, 1.18 mm, 850 microns, 600 microns, 425 microns, 355 microns, 300 microns, 212 microns, 180 microns, 125 microns, 106 microns, 75 microns, and 45 microns). Any fragments that were less than 45 microns were weighed together and noted. After each shot, all fragments were collected, weighed together, and then sieved to determine their distribution. These masses were then converted into a continuous probability density function in which each sieve covered the range between itself and the next highest sieve. Some amount of material was compressed against the anvil and not ejected laterally; in this case, the recompressed fragment was removed and weighed separately.

V. TEST RESULTS AND ANALYSIS

A. INITIAL TEST CONDITIONS

Before the conduct of the impact test, measurements were taken for all samples. The sample dimensions are listed in Table 2 and information on the shot parameters are listed in Table 3.

Table 2. Sample dimensions.

Name	Material	Mass (g)	Diameter (mm)	Height (mm)	Porosity (%)
46–54-S1	Alumina	3.2861	16.25	6.43	46
60–40-S1	Alumina	3.6755	15.84	11.78	60
75–25-S1	Alumina	2.7033	15.82	14.30	75

Table 3. Shot table.

Name	Impactor Mass (g)	Breech Pressure (psi)	Estimated Impactor Velocity (m/s)	Striker Mass (g)	Rubber Insert Thickness (mm)	Estimated Striker Velocity (m/s)
46–54-S1	479.8	102	103	1248.8	6.500	39.6
60–40-S1	479.4	100	102	1266.7	5.922	38.6
75–25-S1	479.7	99	101	1258.2	5.939	38.5

B. FRAGMENT DISTRIBUTIONS

We next consider the experimental fragment distributions for our samples, which represent some of the key data for this thesis. Distributions are given as a mass PDF over a linear size; experimental data points are given at the midpoint of each sieve size and are normalized to the total mass recovered after each individual shot. For shot 46–64-S1, an additional 1.441% of mass was recovered after sieving, with the increase due to a small

amount of contaminants present during the sieving process. Extra precaution was taken to ensure the sieves were thoroughly cleaned prior to the sieving process to mitigate this outcome. The data for all three low velocity gas gun shots is shown in Figure 16, where the solid lines represent a fit to experimental data with a Lineau distribution and symbols represent experimental data points. All plots except that of the 46% porosity are shifted upwards for clarity. The Lineau distribution provides a good fit to the fragment distribution for all three samples. Each fragment distribution shows a distinct maximum and the average fragment size decreases as the porosity of the sample increases. All three distributions shows peaks in the general range of 100 μm; in the sections below we develop a model for predicting the average fragment size, which is in good agreement with the experimental fit values shown in Figure 16.

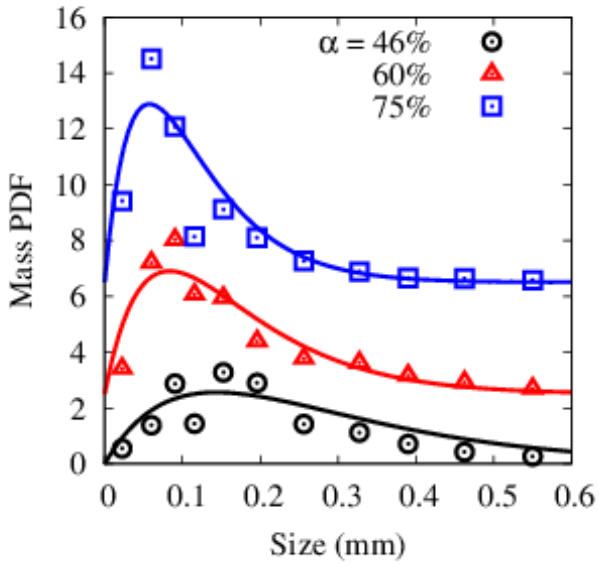

Figure 16. Mass PDF vs. size for freeze cast material with different porosity.

C. MICROSTRUCTURE ANALYSIS OF FRAGMENTS

The fragments collected from the impact test were examined under SEM to determine typical fracture patterns and fragment morphology. Our main goal is to assess how a freeze-cast matrix might behave under the rapid loading that would occur in high-

velocity impact or explosive loading. In the SEM micrographs, we attempted to identify any characteristic fracture behavior, such as trans- or intergranular cracking, crack bridging, and blunting.

Delamination of the layers and fragmentation across the lamellae (perpendicular to the longest direction of the lamellae) were common features for all three samples with different porosities. Delamination of the layers occurred at the intersection of adjacent lamellae, which were deemed to be the weakest link in the lamellar structure. On each lamella, the cracks almost always propagated across the lamellar width, slicing the lamella into smaller fragments. This was evident on the fragments where the broken edges were commonly perpendicular to the direction of the dendritic ridges. The dendritic features of the ice-templated samples run parallel to the direction of growth of the lamella. Figure 17 shows a representative 4.75 mm fragment for the 46% porosity sample where delamination occurred at the broken edges and cracks were observed to be propagating across the lamellae.

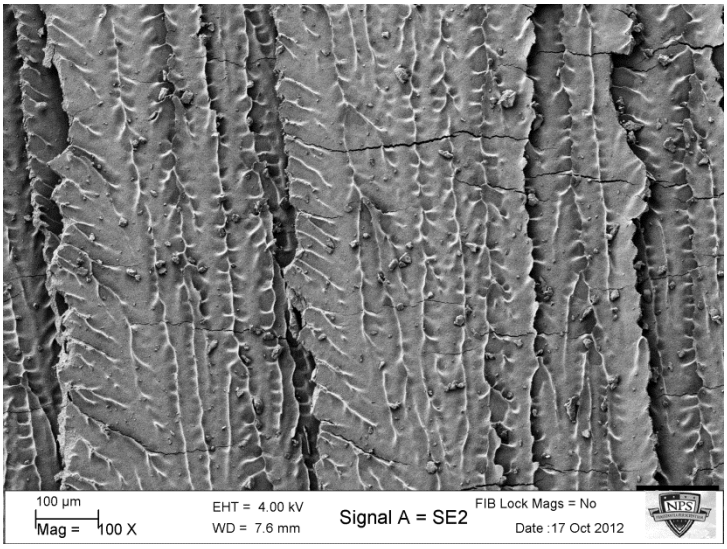

Figure 17. SEM micrograph of 4.75mm fragment for porosity of 46%.

The lowest porosity sample was observed to have a higher surface roughness on the side of the lamella with dendritic features when compared to the samples with 60% and 75% porosity (Figure 18). The surface roughness of the lamellae decreases with

increasing porosity. The 46% porosity sample fragments also displayed fewer cracks across the fragments; in those cases where cracks did propagate, frequently the crack would blunt as it was crossing a dendritic ridge on the rough surface (Figure 19). This further supports the idea that lamellae with a rough surface may reduce the probability of complete crack propagation across the structure and result in a larger average fragment size. The larger number of cracks across the higher porosity sample, as observed in Figure 18(c), is consistent with this idea and with the smaller average fragment dimension observed experimentally.

In Figure 20 we present fragment edges, showing sections of exposed fracture surface from fragments with a relatively smooth and flat grain structure. These fracture surfaces generally have a transgranular character, but very often a mixture of trans- and intergranular failure was also observed. Crack bridging was also commonly observed in many samples. We note that in these highly heterogeneous samples a wide variety of loading conditions and strain rates may occur, and thus drawing general conclusions from individual cracks is challenging.

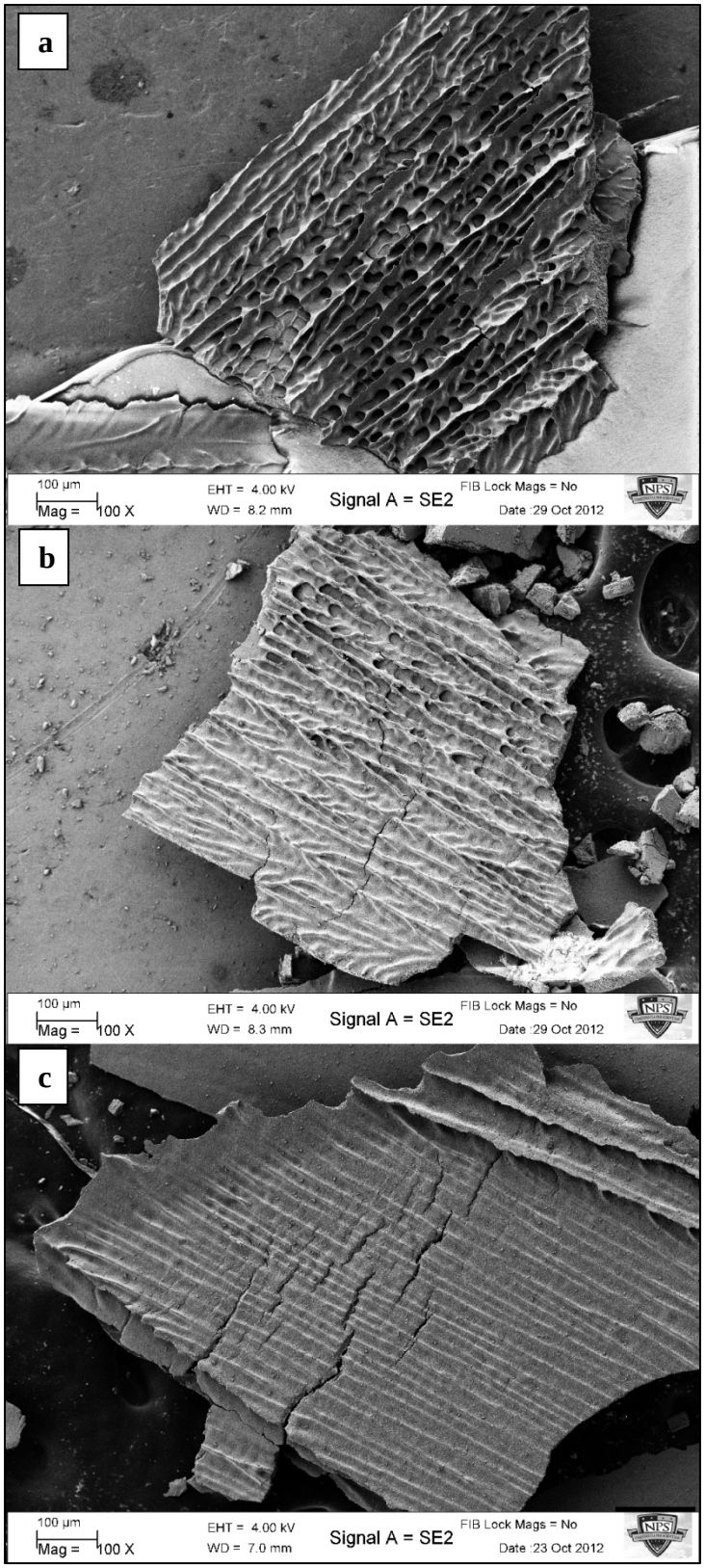

Figure 18. SEM micrograph of 500µm fragment for porosity α = (a) 46% (b) 60% (c) 75%.

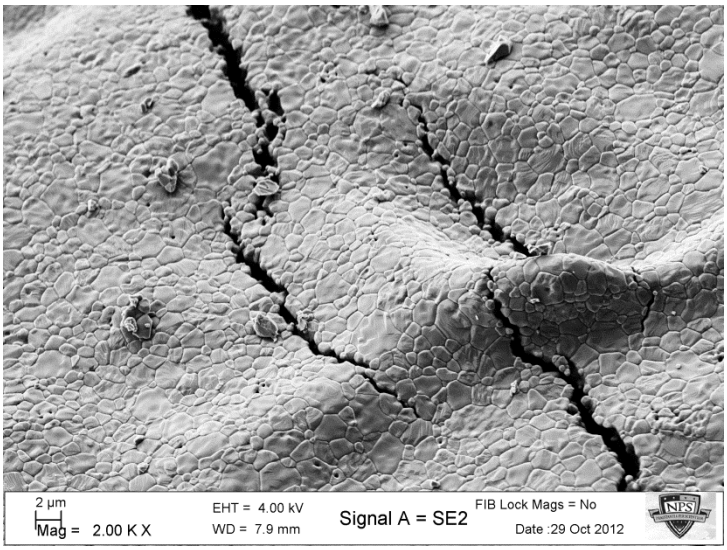

Figure 19. SEM micrograph of 500µm fragment for sample of porosity $\alpha = 46\%$ showing crack bridging and blunting at a dendritic ridge.

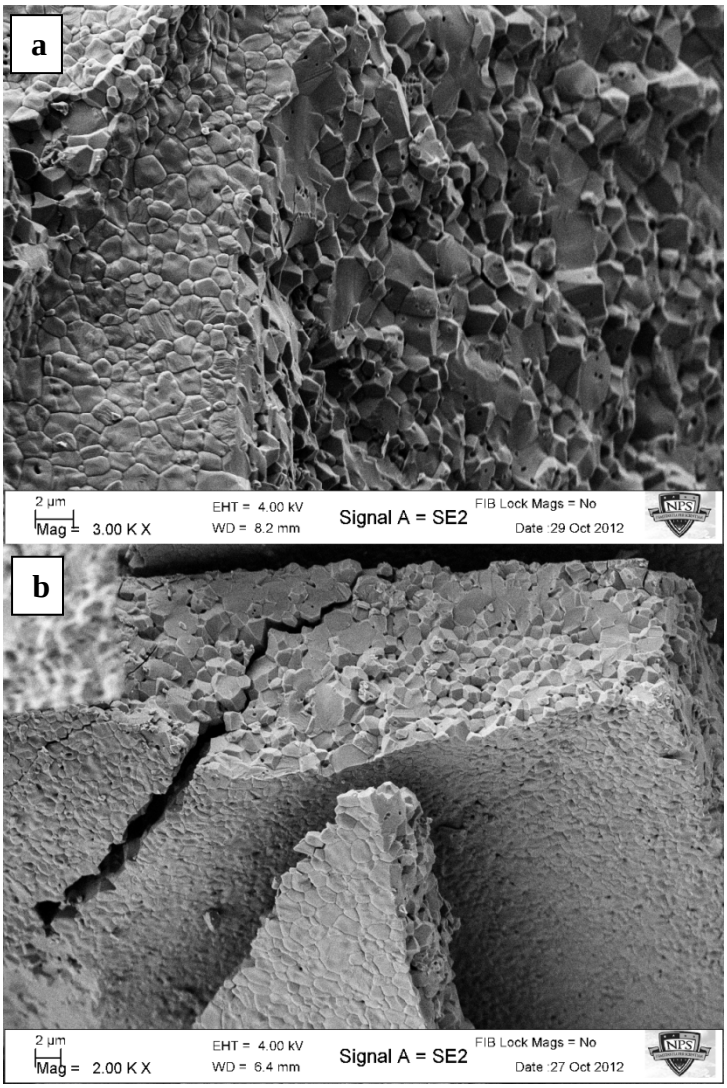

Figure 20. SEM micrograph of (a) 500µm fragment for sample of porosity $\alpha = 46\%$ (b) 55µm fragment for sample of porosity $\alpha = 75\%$. Multi-mode cracking mechanism is observed.

D. FRAGMENTATION MODEL

Based on the morphological features discussed above, we now consider a simple analytic model for the fragmentation of these ice-templated alumina structures under dynamic loading. We assume that under loading the majority of the lamella separate at junction interfaces, and that the measured fragmentation distribution is primarily related to crack initiation and merging across the lamellar width. A schematic of our model is given in Figure 21, where we assume tensile plane stress on the lamella and a candidate cylindrical fragment of radius *a* within the lamella.

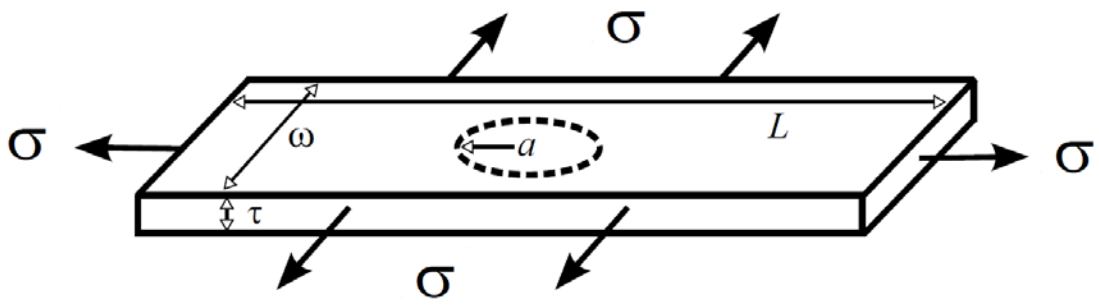

Figure 21. Schematic of the energy balance model for a cylindrical fragment formed within a detached lamella.

We assume, with Grady[11], that the relevant kinetic energy for a candidate fragment is the motion relative to its center of mass. This local kinetic energy is balanced against two additional terms: first, the surface energy required to create *N* cylindrical fragments out of the lamellar structure. Second, we must consider the strain energy as the lamella expands in tension; we assume that fragmentation begins at a critical stress σ_c which is related to the tensile strength of the lamellar material (in our case, bulk alumina). We first consider the local kinetic energy *T*. A cylindrical shell at a distance *r* from the center of a candidate fragment has a mass of

$$dm = 2\pi r \tau \rho dr ,$$

where ρ is the ceramic bulk density and τ is the lamellar thickness. Its kinetic energy can be written as

$$dT = \frac{1}{2}\dot{r}^2 dm,$$

where the expansion velocity $\dot{r}$ can be given in terms of a density expansion rate $\dot{\rho}$,

$$\dot{r} = -\left(\frac{\dot{\rho}}{2\rho}\right) r.$$

The total kinetic energy of a collection of $N = L\omega/\pi a^2$ in a lamella of length *L* is given as

$$T = N\int_0^a dT = \frac{1}{\pi} L\omega\tau\rho\left(\dot{\varepsilon} a\right)^2$$

where we have introduced the strain-rate, $\dot{\varepsilon} = -\dot{\rho}/2\rho$. We assume, following Glenn and Chudnovsky[12], that there is no residual strain remaining in the newly formed fragments after fracturing. The initial strain energy density is

$$U_o = \frac{\sigma_c^2}{E}(1-\nu).$$

Thus the total elastic strain energy available for fragmentation can be written

$$U = \frac{L\omega\tau}{E}\sigma_c^2(1-\nu),$$

where *E* is the Young's modulus of bulk alumina and *v* is its Poisson's ratio. Finally, we consider the change in surface energy when the lamella is broken into a collection of *N* cylindrical fragments. The initial surface energy is given by

$$\Gamma_i = S_a\gamma,$$

where γ is the specific surface energy $\gamma = K_{ic}^2/2\rho c^2$, S_a is the total surface area of the unfractured lamella, and K_{ic} is the static fracture toughness. The total residual surface energy Γ_{res} when *N* cylindrical fragments of radius *a* are formed is

$$\Gamma_{res} = N\Gamma_n = \frac{L\omega\gamma}{\pi a^2}\left(2\pi a\tau + 2\pi a^2\right).$$

The equilibrium fragmentation condition is given by a balance of these four energies,

$$T + U + \Gamma_i = \Gamma_{res}.$$

Substituting the respective energy equations in gives the following cubic equation

$$a^3 + \left[\frac{4\sigma_c^2 (1-\nu)}{E\rho\dot{\varepsilon}^2} + \frac{8\gamma}{L\rho\dot{\varepsilon}^2} + \frac{8\gamma}{\omega\rho\dot{\varepsilon}^2} \right] a - \frac{8\gamma}{\rho\dot{\varepsilon}^2} = 0.$$

Solving the above equation for the equilibrium fragment size *a* yields

$$a = \frac{\kappa - \beta^2}{\beta}$$

where

$$\beta = \left(\lambda + \sqrt{\lambda^2 + \kappa^3} \right)^{1/3}$$

$$\lambda = -2\left(\frac{K_{ic}}{\rho c \dot{\varepsilon}} \right)^2$$

$$\kappa = \frac{4}{3\left(\rho c \dot{\varepsilon}\right)^2} \left[\sigma_c^2 (1-\nu) + K_{ic}^2 \left(\frac{L+\omega}{L\omega} \right) \right].$$

We assume that the critical stress σ_c is equal to the tensile strength of the alumina material, which should be suitable in the case where widespread delamination occurs. The lamellar length *L* is very large compared to the average fragment size, and based on our observations we assume it is comparable to the overall sample dimensions (16 mm). The other lamellar dimensions, the thickness τ and the width ω, both decrease in a similar manner with increasing porosity (see Figure 10). The ratio between them appears to be roughly constant in our recovered fragments, and thus we assume that $\omega/\tau = \xi$, where the constant ξ is approximately 20 for these particular ice-templated alumina structures. The strain rate at the lamellar level was estimated using a simple three-point bending strain,

$$\dot{\varepsilon} = \frac{6\tau v_s}{\omega^2},$$

where v_s is the striker velocity determined based on the conservation of momentum of the impactor on the striker bar. The strain rate values derived from this equation were in the range of 10^4 to 10^5, which are deemed to be reasonable for a dynamic loading.

In Table 4 we present the alumina material properties used in this work. With these parameters, we made use of the fragmentation model to estimate the average fragment size of the freeze-cast specimens.

Table 4. Material properties used in the fragmentation model.

Property	**Value**
Bulk alumina density ρ	3.984 g/cm^3
Sound speed c	10.2 km/s
Fracture toughness K_{ic}	3 MPa$\sqrt{m}$
Poisson's ratio v	0.231
Critical stress σ_c	267 MPa

We first consider the variation in average fragment size with the lamellar width, which has a direct relationship to porosity. The width dependence is plotted in Figure 22. As the lamellar width increases, the average fragment size increases and eventually the curve flattens off at a fragment size of approximately 160 microns. The experimental values, indicated by the data points on Figure 22, agree very well with the fragmentation model. If these data are representative, this implies that the fragmentation of the freeze cast material can be predicted from the balancing of the energies (surface energy, strain energy and kinetic energy) in the system.

The Lineau fragment size distribution is a reasonable fit to the fragmentation behavior of the material. As observed in the SEM micrographs of the fragments, the cracks randomly slice each lamella across the length, similar to the Lineau one-dimensional model with random breaks and lengths of the segments delineated by these breaks. While additional shots in other orientations are desirable, our initial work suggests that an energy balance model combined with a one-dimensional Lineau

distribution can, with only basic information on the microstructure, predict the average fragment size of ice-templated freeze cast materials under dynamic loading.

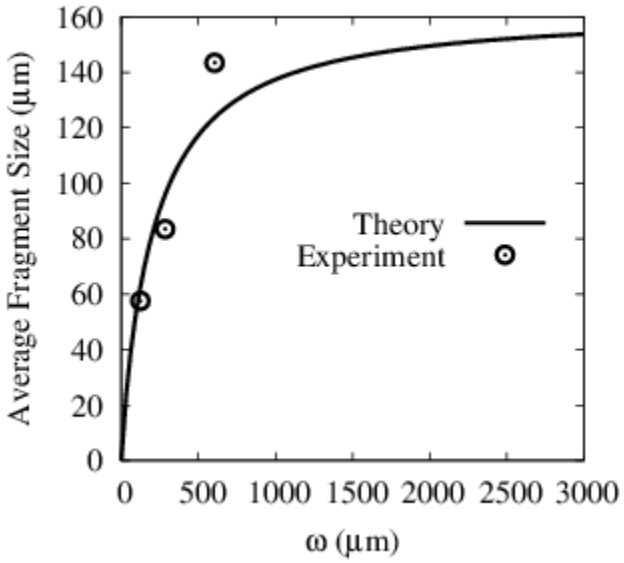

Figure 22. Average fragment size vs. lamellar width ω.

VI. CONCLUSIONS AND RECOMMENDATIONS

A. CONCLUSIONS

The microstructure and fragmentation behavior of ice-templated freeze cast materials were studied as a function of varying sample porosity. The porosity of the material is a direct replica of the solvent content and can be carefully controlled; in addition to a porosity change, however, there are also a range of changes in the microstructure and lamellae comprising the material. Lamellar thickness and width of the freeze cast samples decrease significantly as the porosity of the material increases. Impact tests were performed, and the general fracture trends under dynamic loading are consistent across all porosities; both trans- and intergranular failure are observed, and all samples show nearly complete delamination and cracking across the lamellar width. Recovered fragments were sieved and data points were fit to a Lineau distribution. Though the form of the distribution is the same in all cases, there is a systematic variation in which the average fragment size decreases with increasing porosity.

A theoretical model was developed to predict the average fragment size of the freeze cast alumina material, based on a balance of kinetic, strain, and surface energy. The model predicts that as the lamellar width of the freeze cast sample increases, the average fragment size will increase accordingly. As the lamellar width is closely linked to the sample porosity, it correctly predicts that the lower porosity freeze cast material will have a larger average fragment size.

B. RECOMMENDATIONS

With the material properties and fragmentation model established for plain, unfilled freeze cast materials, more work needs to be done to validate the fragmentation model with filled samples and additional porosities. Additional material testing at the lamellar level is also desirable for our sample, as currently we are using bulk alumina material properties to treat a single lamella in the fragmentation model. With the unique structural properties of the freeze cast matrix, its local fracture toughness may deviate significantly from that of the bulk alumina.

The motivation of this current study is to derive a new form of warhead casing. Freeze cast materials with infiltrated reactive materials could optimize the performance of reactive materials by increasing the surface area of the reactive materials formed. The addition of reactive materials will affect the physical properties of the freeze cast sample due to the combination of ductile and brittle deformation that can occur within the layers. The fragmentation characteristics of infiltrated freeze cast samples should be investigated to determine the suitability of its application in warhead casings.

APPENDIX

C. RAW DATA FOR 46–54-S1 EXPERIMENT

Date:	6-Oct-12
Sample:	46–54-S1
Mass before impact (g):	3.2861
Fragment mass recovered (g):	2.1305
Mass of recompressed sample (g):	0.9122
Total Mass recovered (g):	3.0427
Percentage loss during impact:	7.407%
Mass after sieving (g):	2.1612
Percentage loss during sieving:	-1.441%
Characteristic sample size (mm):	10.00

Sieve size (mm)	Mass in sieve (g)	Midpoint (mm)
4.75	0.1324	7.375
2.8	0.1597	3.775
1.7	0.0627	2.25
1.18	0.059	1.44
0.85	0.0508	1.015
0.6	0.0675	0.725
0.5	0.0587	0.55
0.425	0.0698	0.4625
0.355	0.1083	0.39
0.3	0.1336	0.3275
0.212	0.272	0.256
0.18	0.2008	0.196
0.125	0.3898	0.1525
0.106	0.0592	0.1155
0.075	0.1929	0.0905
0.045	0.09	0.06
0	0.054	0.0225

D. RAW DATA FOR 60–40-S1 EXPERIMENT

Date:	12-Oct-12
Sample:	60–40-S1
Mass before impact (g):	3.6755
Fragment mass recovered (g):	2.2259
Mass of recompressed sample (g):	1.2371
Total Mass recovered (g):	3.4630
Percentage loss during impact:	5.782%
Mass after sieving (g):	2.0905
Percentage loss during sieving:	6.083%
Characteristic sample size (mm):	10.00

Sieve size (mm)	**Mass in sieve (g)**	**Midpoint (mm)**
4.75	0	7.375
2.8	0	3.775
1.7	0.0292	2.25
1.18	0.0136	1.44
0.85	0.0289	1.015
0.6	0.047	0.725
0.5	0.0411	0.55
0.425	0.0673	0.4625
0.355	0.0967	0.39
0.3	0.1291	0.3275
0.212	0.2337	0.256
0.18	0.1268	0.196
0.125	0.3962	0.1525
0.106	0.1416	0.1155
0.075	0.358	0.0905
0.045	0.2954	0.06
0	0.0859	0.0225

E. RAW DATA FOR 75–25-S1 EXPERIMENT

Date:	17-Oct-12
Sample:	75–25-S1
Mass before impact (g):	2.7033
Fragment mass recovered (g):	1.3550
Mass of recompressed sample (g):	1.0113
Total Mass recovered (g):	2.3663
Percentage loss during impact:	12.466%
Mass after sieving (g):	1.2714
Percentage loss during sieving:	6.170%
Characteristic sample size (mm):	10.00
Mass of recompressed sample (g):	1.2

Sieve size (mm)	**Mass in sieve (g)**	**Midpoint (mm)**
4.75	0	7.375
2.8	0.0375	3.775
1.7	0.0793	2.25
1.18	0.0103	1.44
0.85	0.0039	1.015
0.6	0.0106	0.725
0.5	0.0101	0.55
0.425	0.0128	0.4625
0.355	0.0142	0.39
0.3	0.0269	0.3275
0.212	0.086	0.256
0.18	0.065	0.196
0.125	0.1832	0.1525
0.106	0.0398	0.1155
0.075	0.2198	0.0905
0.045	0.3053	0.06
0	0.1667	0.0225

THIS PAGE INTENTIONALLY LEFT BLANK

LIST OF REFERENCES

[1] D. Grady, *Fragmentation of Rings and Shells* (Springer, Germany, 2006), 1st ed.

[2] J. P. Hooper, J. Appl. Phys. **112**, 043508 (2012).

[3] J. A. Astrom, F. Ouchterlony, R. P. Linna, and J. Timonen, Phys. Rev. Lett. **92**, 24 (2004).

[4] E. Sharon, S. Gross, and J. Fineberg, Phys. Rev. Lett. **76**, 12 (1996).

[5] R. Wilson, M. Sci. Thesis, Naval Postgraduate School, 2012.

[6] S. Deville, Adv. Eng. Mater. **10**, 155 (2008).

[7] E. Munch et al., Science **322**, 1516 (2008).

[8] S. Deville, E. Saiz, R. K. Nalla, A. P. Tomsia, Science **311**, 515 (2006).

[9] T. Fukasawa, Z.-Y. Deng, M. Ando, T. Ohji, Y. Goto, J. Mater. Sci. **36**, 2523 (2001).

[10] S. Deville, E. Saiz, A. P. Tomsia, Acta Mater. **55**, 1965 (2007).

[11] D. Grady, J. Appl. Phys. **53**, 322 (1982).

[12] L. A. Glenn, A. Chudnovsky, J. Appl. Phys. **59**, 1379 (1986).

THIS PAGE INTENTIONALLY LEFT BLANK

INITIAL DISTRIBUTION LIST

1. Defense Technical Information Center
   Ft. Belvoir, Virginia

2. Dudley Knox Library
   Naval Postgraduate School
   Monterey, California

3. Joseph P. Hooper
   Naval Postgraduate School
   Monterey, California

4. John Molitoris
   Lawrence Livermore National Laboratory
   Energetic Materials Center
   Livermore, California